Materials Science & Engineering A 863 (2023) 144526

Contents lists available at ScienceDirect

Materials Science & Engineering A

journal homepage: www.elsevier.com/locate/msea

A novel methodology for the prediction of the stress–strain response of laser powder bed fusion lattice structure based on a multi-scale approach

Pietro Magarò [a,*], Gianluca Alaimo [b], Massimo Carraturo [b], Emanuele Sgambitterra [a], Carmine Maletta [a]

[a] Department of Mechanical, Energy and Management Engineering, University of Calabria, Rende (CS), 87036, Italy
[b] Department of Civil Engineering and Architecture, University of Pavia, via Ferrata 3, Pavia (PV), 27100, Italy

ARTICLE INFO

Keywords:
Laser powder bed fusion
Nano-indentation
Finite element analysis
Micro-CT
Stainless steel 316L

ABSTRACT

Additive manufacturing (AM), and in particular laser powder bed fusion (LPBF), is a technology that allows to easily produce geometrically complex structural components. Among others, an example is represented by lattice structures which allow to obtain lightweight components with enhanced mechanical properties. Despite a large number of papers available in the literature, mechanical behavior of lattice structures made by LPBF is still difficult to predict, due to microstructure modifications induced by their small features, scanning strategy and building direction. In this regard, a multi-scale approach to predict the effective $\sigma - \epsilon$ response within the lattice structure is proposed in this investigation. It mainly consists in local measurements by nano-indentation tests, carried out at different portion of the lattice structure and along different orientation to build the effective constitutive response of the component. In this way, possible modifications induced by the LPBF process within the microstructure can be captured. Relying on experimental investigations at both macro and nano-scale, a numerical model for stainless steel 316L octet-truss lattice specimen has been calibrated. To improve the accuracy of the simulations, the geometrical model was built starting from the real geometry of the component through μ-CT images. Obtained results revealed that using the as-built geometry and effective local properties is fundamental for an accurate prediction of the mechanical behavior of lattice structures made by LPBF manufacturing process.

1. Introduction

Additive manufacturing (AM), and in particular laser powder bed fusion (LPBF), is a manufacturing process that is arousing great interest among the scientific and industrial community since it allows to produce complex components with custom geometries that are impossible to realize with traditional subtractive technologies. A very interesting example are lattice structures [1,2], that are three-dimensional networks of unit cells characterized by high specific strength as well as high energy absorption capacity, that allow to obtain lightweight components with high mechanical properties [1,3,4].

In the last years, a lot of studies have been conducted on lattice structures of Ti–6Al–4V obtained by additive manufacturing [1,5], since it is characterized by high strength and corrosion resistance; however, stainless steel 316L (SS 316L) represents a good alternative [6,7] thanks to its lower cost, higher ductility, and lower sensitivity to residual stress and cracking if compared to Ti–6Al–4V [5].

In any case, a technical issue arising in the LPBF process is given by the presence of defects induced by the process parameters, as well as the surface roughness [8], especially when they are subjected to cyclic loads. For industrial applications, it is extremely important to know how such defects could affect the mechanical properties and anisotropy of LPBF components. Additionally, it is important to take into account that printing strategies often are responsible for the formation of surface defects.

Lack of fusion defects can be induced by an insufficient distance of two adjacent scanning lines, as these conditions imply the presence of particles not completely fused [8]. Moreover, also the presence of unstable melt pools can be considered as a reason for the formation of such defects. This phenomenon can be attributed to the recoil pressure based on to the Marangoni effect [9,10] since the formed melt pools are exposed to high cooling rates. A decrease in the energy density can help to overcome this technical issue, but in this way a further increase in porosity could be obtained as a consequence of the not completed fusion of the powder.

Also for LPBF lattice structures printing strategies can affect the mechanical behavior, leading to a different response if compared to

* Corresponding author.
E-mail address: pietro.magaro@unical.it (P. Magarò).

https://doi.org/10.1016/j.msea.2022.144526
Received 31 July 2022; Received in revised form 16 December 2022; Accepted 20 December 2022
Available online 22 December 2022

the bulk material obtained with the same process. In this regard, several works analyzed how geometrical defects affect the mechanical properties of the lattice structures. Additionally, different static and fatigue properties along directions parallel and perpendicular to the building direction were observed [6,11–15].

A fine microstructure usually characterizes LPBF materials if compared with conventional material. Printing strategies imply high cooling rates, repeated thermal cycling, and varying thermal gradients during layer-by-layer melting, together with a high-power laser. These latter, usually, lead to complex nonequilibrium microstructures [16,17]. Therefore, it can be assessed that typical cellular microstructure, observable in LPBF SS 316L, can be considered as a consequence of the complex thermal history that results in non-equilibrium conditions during solidification.

Moreover, non-uniform solidification of the material leads to a constitutional supercooling/undercooling within the liquid and a rejection of solute into the cell walls, in this case primarily Mo and Cr [18–24]. The consequent increase of these elements results in a melt pool densely populated with geometrically necessary dislocations, and the consequent dislocation locking as a key factor of the high strength of the components obtained by LPBF [17–20,22,25–27].

Several authors [28–32] highlighted how in FCC crystals, columnar cells tend to grow along the ⟨100⟩ directions and, in particular, along the maximum thermal gradient that is perpendicular to the melt pool boundary. Epitaxial growth often occurs in the crystal below the melt pool and in the same direction of the thermal gradient (primary) or in a secondary growth direction, that is perpendicular to the primary direction [17,21,22,24,28–34]. As a consequence, grains tend to be elongated along the vertical building direction

In addition, it was observed that reducing the mismatch angle between the epitaxial direction and maximum thermal gradient the growth preferences change, modifying the grain morphology significantly. As a consequence, the variation of the scanning strategy could imply a ⟨100⟩ or ⟨110⟩ texture preference along the building direction. This phenomenon is based on the effect of the weld pool stacking on the thermal gradient and on the mismatch angle. These latter, in fact, tend to modify the weld pool shape and the relative location, and can be controlled by processing parameters such as power, speed, and hatch spacing [28,32].

Several studies were carried out for optimizing design of LPBF lattice structures in terms of relative density, unit size, unit geometry, trusses length, and truss thickness [35]. Finite element analyses are widely used to estimate the mechanical properties of complex lattice structures with varying their characteristics parameters. However, these methods are often not experimentally validated as the same and isotropic bulk mechanical properties are assumed for trusses and nodes. Microstructural alterations, together with significant differences between as-designed and as-built geometry in terms of surface roughness lead to not negligible mismatch between numerical and experimental results [36].

Moreover, several authors observed that changes in the available heat amount has a significant effect to the LPBF SS 316L microstructure. In this regard, Piazza et al. [37] using cylindrical and conical bulk SS 316L sample, with equal base diameters, observed that the hardness of the cylindrical sample was more sensitive to the modification of the process parameters. The upper layer of the cylindrical sample, having a larger area, requires higher overall heat amount, which exceed the heat extraction capacity of the geometry below, so when higher energy process parameters were adopted, the cylindrical part underwent more drastic heat accumulation which resulted in a slower cooling rates. Similarly, Mohr et al. [38] demonstrated that the feature geometry can reduce the heat flow and consequently modifies the microstructure. Wang et al. [27] showed a transition from ⟨110⟩ to ⟨100⟩ texture in vertical trusses with a thickness smaller than 0.25 mm, due to changes in heat flow.

However, few investigations are available about the local microstructure modification in the case of inclined trusses, and about the role played by different process on these modifications. This is extremely important in trusses with a diameter smaller than 1 mm, as they are more affected by edge effects. Furthermore, there are limited studies on the formation of sub-structures in nodes and thin trusses.

Micrographic analysis allows to evaluate the microstructure of the material and how it is affected by printing strategies.

A possible non-destructive method to identify the presence of pore/defects inside the sample and to reconstruct the real morphology obtained after the manufacturing process is the use of X-ray micro-computed tomography (μ-CT). In addition, μ-CT is widely used for density measurements of different AM materials such as aluminum [14,39,40] and titanium alloys [41,42]. However, due to the high density, high absorption coefficient, and the effect of beam hardening, that could lead to artifacts and/or noise in the μ-CT data, steel represents an open challenge for X-ray analysis. In any case, results obtained by μ-CT analysis can be used to identify critical pores or defects and to analyze their size, shape and position.

Also the as-built geometry, resulting after LPBF process, can be measured through a micro-computed tomography (μ-CT), providing an input model for numerical simulations [43]. To date, numerical simulations are mainly used in order to optimize the LPBF process parameters with the aim to minimize process-induced defects [44–46]. In fact, due to the non negligible differences between as-designed and as-built geometry, mechanical Finite Element Analysis (FEA) has to be performed on the geometrically challenging as-built model, hindering a straightforward adoption of FEA-based mechanical characterization of LPBF lattice structures.

For example, Boniotti et al. utilized 3D tomography in order to show how defects in a body-centered cubic (BCC) lattice structure are responsible to local strain concentrations that lead to poorer strength [47,48] or fatigue resistance [49].

Another fundamental task when lattice structures are analyzed by Finite Element Method (FEM) is represented by the assigned material properties. In the case of LPBF lattice structures, in fact, the analysis at different geometrical scales is required, since the mechanical properties obtained from monotonic tensile tests are not enough for the characterization of the material. For these kind of applications, in fact, small-scale tests are necessary to capture the material behavior at the microstructure level. Recent studies in nano-mechanical sensing and micro-fabrication allowed to characterize bulk materials at small scales [50–52]. A detailed understanding of the micro-mechanical response provides insight into the fatigue and fracture mechanisms, facilitating a better explanation of the experimental evidence. Roos et al. [53] performed nano-indentation experiments on LPBF SS 316L lattice parts and observed a significant size effect. In particular, they found an increase of the hardness from about 4 GPa to 6 GPa as the indentation depth decreased from 500 nm to 50 nm. This behavior is caused by the scaling of the geometrically necessary dislocations under the indenter [54].

In the present study a novel approach to predict the mechanical response of lattice structure made by LPBF SS 316L is proposed. In a previous work by the authors [55], it was found that bulk mechanical properties cannot be used to calibrate an accurate constitutive material model for lattice structures, even using the as-built geometry obtained by μ-CT images. The higher than usual cooling rates, in fact, directly affects the resulting microstructure, that was also analyzed. As a consequence, $in-situ$ measurements are necessary in order to understand how microstructure modifications affect the material response. Nano-indentation technique provides a fast and practical approach for the determination of the effective mechanical properties. With this purpose, local measurements were carried out to estimate the stress–strain response on the two characteristic zones of the lattice sample, i.e. a truss and a node, and in both planes, i.e. parallel and perpendicular to the building direction.

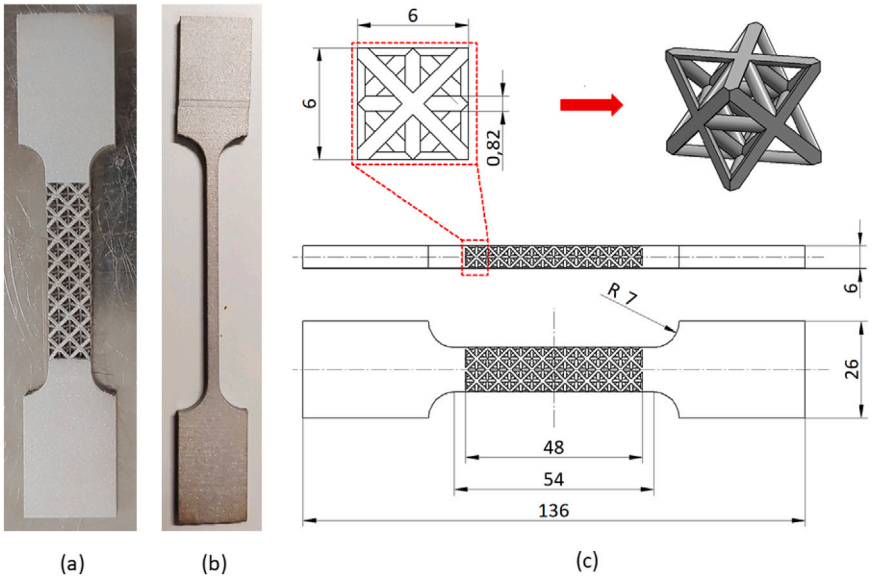

Fig. 1. Lattice and bulk specimens: (a) as-built lattice sample, (b) as-built bulk sample, (c) geometry of the lattice specimen and of the octet-truss cell with the main dimensions.

Table 1
Main process parameters used for the manufacturing of lattice and bulk specimens.

Process parameter	Value
Build plate temperature	170 ± 1 °C
Chamber temperature	35 ± 5 °C
Layer thickness	50 ± 1 μm
Hatch spacing	110 ± 2 μm
Laser spot	70 ± 1 μm
Scan speed	1200 ± 2 mm/s
Laser power	200 ± 0.1 W

Table 2
Chemical composition of SS 316L powder (weight percent).

Fe	Cr	Ni	Mo	Mn	Si	N	O	C	S	P
16–18	10–14	2–3	≤2	≤2	≤1	≤0.1	≤0.1	≤0.03	≤0.03	≤0.045

2. Materials and experiments

2.1. Manufacturing

Four specimens were printed for both lattice (Fig. 1(a)) and bulk (Fig. 1(b)) samples with stainless steel 316L metal powder (SS316L-0447 Renishaw) using a Renishaw AM400 SLM additive manufacturing system available at the 3DMetal@UniPV Laboratory of the University of Pavia. Table 1 reports the adopted process parameters.

Table 2, instead, reports the chemical composition, provided by the supplier, for SS 316L powder.

The as-designed lattice specimen was obtained from a calibrated zone characterized by a 8 × 2 grid of equally-spaced octet-truss cells with equal sides of 6 mm length and a density of 20%, which leads to a truss diameter of 0.82 mm, as shown in Fig. 1(c). After the support removal, the geometry of one lattice specimen was acquired using a μ-CT scan, in order to observe the geometrical and material defects present in the structure. The μ-CT data acquisition was conducted with a Phoenix V|tome|x C (Waygate Technologies) machine setting a voxel resolution of 32 μm.

Fig. 2(a) shows the geometry reconstructed from μ-CT images, and overimposed to the CAD design. The comparison refers to the central row of the lattice portion of the specimen. From a qualitative point of view, several geometrical irregularities were observed on the down-skin zones, i.e. on the surfaces opposite to the build direction. Such irregularities are mainly due to partially melted powder particles that remain attached to the specimens surfaces, even after sandblasting process. Moreover, light to moderate bending of the trusses was observed, with the curvature contained in a plane parallel to the building direction.

Fig. 2(b) represents the contour plot of the distances between corresponding points on the as-built and as-designed geometries, carried out through the Autodesk Netfabb software. This analysis allowed to evaluate the geometrical error distribution of the as-built lattice. More in detail, an average distance of almost 60 μm was found, whereas the histogram presented in Fig. 2(c) shows that the most frequent error measure is in the range $[0, 100]$ μm.

2.2. Microstructure analysis

Microstructural characterization of AM samples was carried out by light micrographic (LM) investigations (DM4000 M, Leica, Germany). Both trusses and nodes of the lattice sample were observed. Furthermore, longitudinal and transverse sections, i.e., parallel and perpendicular to the building direction, were analyzed in order to capture possible anisotropies induced by the LPBF scanning pattern on the microstructure morphology. The LM samples were cut, mounted using epoxy resin, grinded with wet SiC grinding papers and polished by diamond solution and silica both with polishing cloths. The microstructure was revealed by etching with a mixture of acids (50 ml H_2O, 10 g $CuSO_4$ and 50 ml HCl).

2.3. Nano-scale measurements

Nano-indentation tests were carried out by a nano-indenter (NHT, CSM Instruments, Switzerland) equipped with a Berkovich diamond tip and with an indentation load of 100 mN. Matrices of 10 × 10 indentations were made for each investigation region. Nano-indentation results were used to estimate the mechanical properties of the samples at the grain scale as well as to capture possible inhomogeneities and anisotropies resulting from the LPBF scanning pattern. To this aim, longitudinal and transverse sections of both trusses and nodes were analyzed. The microstructure morphology is directly affected by the scanning strategy, and is expected to play an important role on the mechanical response of the indented material. A typical force–displacement ($P - h$) curve obtained from instrumented indentation is illustrated in Fig. 3. The main indentation parameters, i.e. the curvature of the loading path (C), the unloading slope at the maximum indentation depth ($S = \frac{dP}{dh}\Big|_{h_m}$), the maximum ($h_m$), residual ($h_r$) and

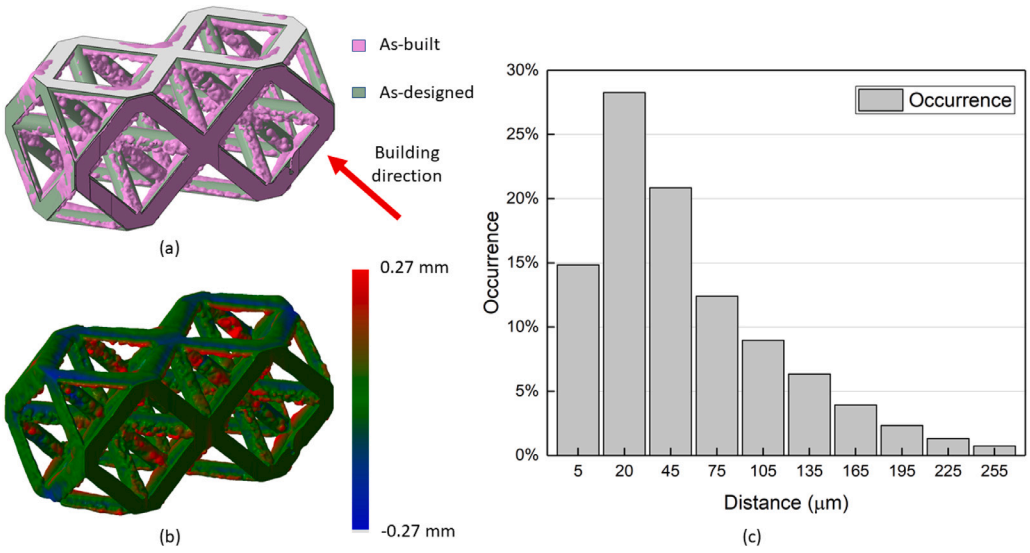

Fig. 2. Comparison between as-built and as-designed geometry: (a) superposition of as-built and as-designed geometries, (b) contour plot of the distance between as-built and as-designed geometries.

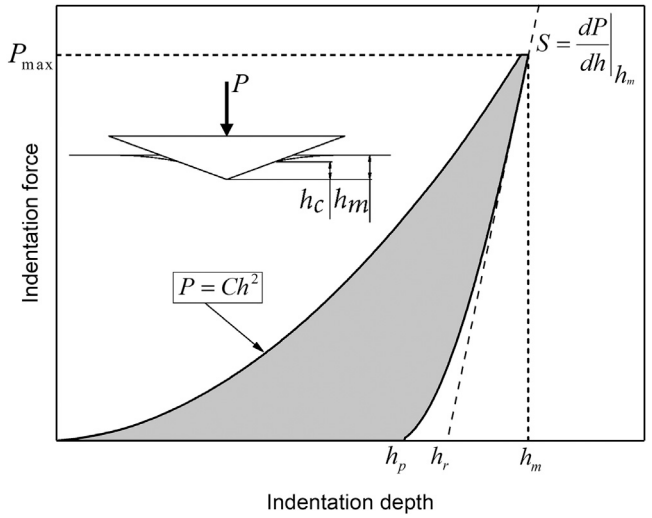

Fig. 3. Instrumented nano-indentation curve: indentation force vs. penetration depth.

permanent (h_p) indentation depths are also shown. The parameter h_c allows to take into account the pile-up or sink-in phenomena and it is measured as the contact depth of the indenter with the sample at the maximum load P_{max}. Such a parameter is geometrically obtained as a function of the residual depth h_r and h_m, through a geometric constant ϵ, that for the Berkovich tip is set to 0.77, according with the following equation:

$$h_c = h_m - \epsilon \frac{P_{max}}{S} \tag{1}$$

These latter parameters were used to estimate the main mechanical properties at the local scale, within both elastic and plastic region, by the approach described in Section 3.1.

2.4. Macro-scale measurements

Tensile tests were carried out on both bulk and lattice samples by an electro-dynamic testing machine (ElectroPuls E10000, Instron, UK) under displacement control, at a cross-head rate of 0.5 mm/min. Sample geometry and dimensions are shown in Fig. 4(a). Bulk material properties of additively manufactured SS 316L were measured from dog bone samples, with a cross section of 3 mm × 3 mm and a length of the reduced parallel section equal to 60 mm. In both cases strain evolution was recorded using an extensometer with a gauge length equal to 10 mm for the bulk sample and 45 mm for the lattice sample. In particular, this latter value was chosen in order to take into account the effect of the entire zone characterized by lattice structures. Both elastic modulus (E) and yield strength (σ_y) were directly obtained from the measured stress–strain ($\sigma - \epsilon$) curve. The equivalent mechanical properties of the octet-truss lattice structure were measured at the macro scale by the dog bone sample shown in Fig. 4(b). *In − situ* digital image correlation (DIC) analyses were also carried out to capture local deformations on both trusses and nodes. Digital images were recorded by a high resolution digital camera (Sony ICX 625 - Prosilica GT 2450 model), 2448 × 2050 pixels). The focus was obtained using a Linos Photonics objective and a Rodagon lens f. 80 mm with a proper magnification, allowing a scale of 380 pixels/mm. This allows to capture an entire unit cell of the octet-truss lattice structure, that is composed by one node and neighboring trusses, as shown in Fig. 4(c). The figure also shows a schematic depiction of the experimental setup used for the correlation analyses.

Correlation analyses were carried out by commercial software (Vic-2D, Correlated Solution), using a subset size of 51 pixels and a distance of 5 pixels between subsets centers.

3. Modeling

3.1. Constitutive model

The whole stress–strain constitutive relation of AM material was estimated at the local scale from nano-indentation results in both elastic ($\sigma \leq \sigma_y$) and plastic ($\sigma > \sigma_y$) regions:

$$\sigma = \begin{cases} E\epsilon & \sigma \leq \sigma_y \\ \sigma_y \left(1 + \frac{E}{\sigma_y}\epsilon_p\right)^n & \sigma > \sigma_y \end{cases} \tag{2}$$

The plastic branch of the stress–strain curve is modeled by the power law Eq. (2), where n is the strain hardening exponent and ϵ_p the plastic component of the total effective strain.

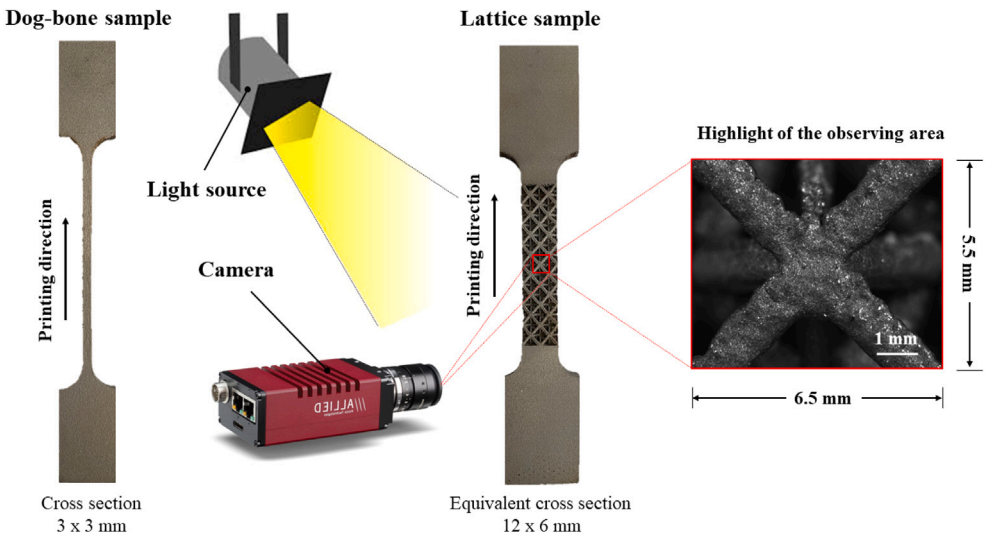

Fig. 4. Sample geometry and main dimensions together with a schematic depiction of the experimental setup used for the digital image correlation analysis.

3.1.1. Elastic model

The Young's modulus E, reported in Eq. (2), was obtained from the slope of the unloading path of the nano-indentation curve. In particular, the reduced Young's modulus E^* can be directly calculated (see Fig. 3) according to the standard ISO 14577-1 (2002) [56] based on the Oliver and Pharr (1992) method [50], by the following equation:

$$E^* = \frac{S}{2\beta}\sqrt{\frac{\pi}{A(h_c)}} \tag{3}$$

where $A(h_c)$ is the projected area at the contact depth h_c, and β is a constant equal to 1.034 for the Berkovich tip. The indentation modulus of the material, E, can be obtained from E^* as follows:

$$\frac{1}{E^*} = \frac{1-\nu^2}{E} + \frac{1-\nu_i^2}{E_i} \tag{4}$$

where ν, E, ν_i and E_i are the Poisson's ratio and the Young's modulus of the material and the indenter, respectively.

3.1.2. Plastic flow model

The effective local yield strength σ_y of the samples was estimated starting from the nano-hardness (H) values [57–60], according to the following equation:

$$\sigma_y = kH \tag{5}$$

where the constant k was calculated by comparing the hardness value, obtained from nano-indentation experiments, and the yield strength obtained from uniaxial tensile tests of bulk AM samples. This parameter was used to estimate the local yield strength of the lattice samples from the respective local hardness values. The plastic flow exponent n, see Eq. (2), was also estimated from the nano-indentation curve by the model proposed by Dao et al. [61]. This latter uses the curvature C of the loading path of the indentation response (see Fig. 3), which is correlated to significant parameters of the stress–strain curve through the dimensionless function Π_α as follows:

$$C = \sigma_r \Pi_\alpha\left(\frac{E^*}{\sigma_r}\right) \tag{6}$$

where σ_r is a representative stress that corresponds to a characteristic strain, $\epsilon_r = 0.033$, while E^* is the reduced Young's modulus, see Eq. (3). The representative strain $\epsilon_r = 0.033$ can be identified since the corresponding dimensionless function Π_α, normalized with respect to $\sigma_{0.033}$, was found to be independent of the strain hardening exponent n. This result indicates that, for a given value of E^*, the stress–strain responses that exhibit the same true stress at the plastic strain $\epsilon = 0.033$ give also the same indentation loading curvature C (see Fig. 3). It is noted that this result was obtained within the specified range of material parameters using the material constitutive behavior defined by Eq. (2).

The curvature C is obtained by a fitting of the measured indentation curve, according to the Kick's law [62], that is assuming a quadratic trend of the $P-h$ loading curve:

$$P = Ch^2 \tag{7}$$

The dimensionless function Π_α can be obtained by a polynomial series as follows:

$$\Pi_\alpha\left(\frac{E^*}{\sigma_r}\right) = \frac{C}{\sigma_r} = \alpha_1\left[ln\left(\frac{E^*}{\sigma_r}\right)\right]^3 + \alpha_2\left[ln\left(\frac{E^*}{\sigma_r}\right)\right]^2 + \alpha_3\left[ln\left(\frac{E^*}{\sigma_r}\right)\right] + \alpha_4 \tag{8}$$

where α_i are constant parameters depending on the indenter geometry (see Appendix). The representative stress σ_r is obtained by solving Eq. (8). Once σ_r is obtained, the hardening exponent can be estimated exploiting the unloading path of the force-penetration response of the indentation test. In particular, the slope S at the beginning of the unloading path can be expressed through the dimensionless function Π_β as follows:

$$\left.\frac{dP}{dh}\right|_{h_m} = E^* h_m \Pi_\beta\left(\frac{E^*}{\sigma_r}, n\right) \tag{9}$$

where Π_β is given by:

$$\Pi_\beta\left(\frac{E^*}{\sigma_r}, n\right) = \frac{1}{E^* h_m}\left.\frac{dP}{dh}\right|_{h_m} = (\beta_{11}n^3 + \beta_{12}n^2 + \beta_{13}n + \beta_{14})\left[ln\left(\frac{E^*}{\sigma_r}\right)\right]^3 + (\beta_{21}n^3 + \beta_{22}n^2 + \beta_{23}n + \beta_{24})\left[ln\left(\frac{E^*}{\sigma_r}\right)\right]^2 + (\beta_{31}n^3 + \beta_{32}n^2 + \beta_{33}n + \beta_{34})\left[ln\left(\frac{E^*}{\sigma_r}\right)\right] + (\beta_{41}n^3 + \beta_{42}n^2 + \beta_{43}n + \beta_{44}) \tag{10}$$

where β_{ij} are constant parameters depending on the indenter geometry (see Appendix). The solution of Eq. (10) provides the value of the hardening exponent n.

3.2. Numerical setup

The general purpose implicit finite element software ABAQUS/Standard 2019® [63] has been employed to perform numerical analysis. The actual geometry of the lattice sample was modeled thanks to μ-CT scan acquisition, whereas the mesh geometric tolerance

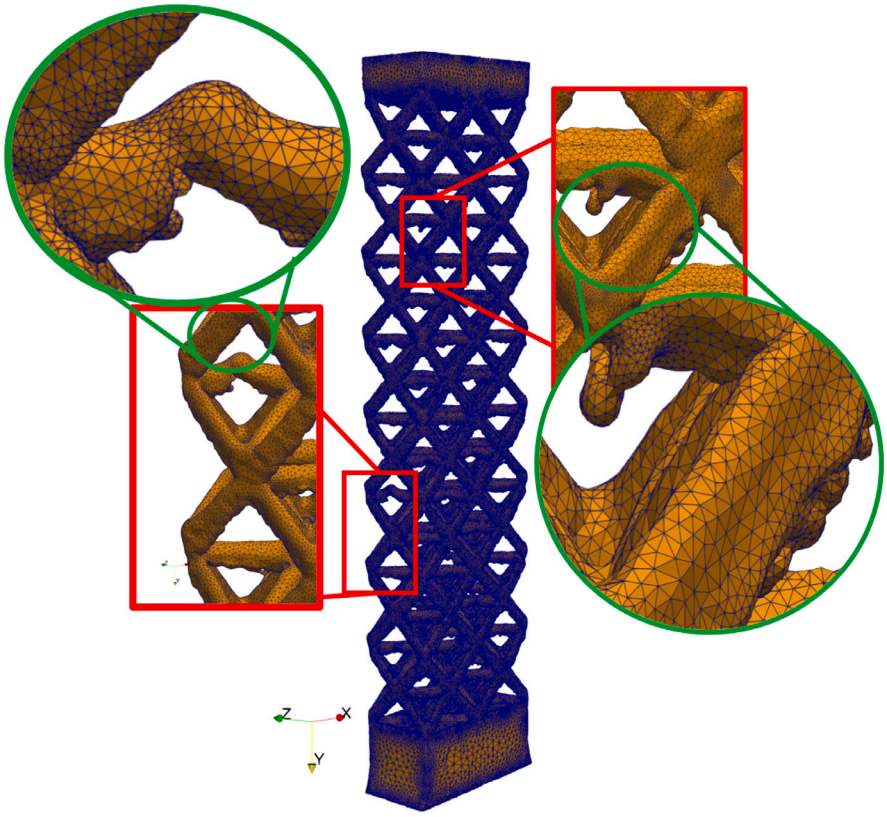

Fig. 5. Finite element discretization of the as-built geometry as acquired by μ-CT with a mesh tolerance equal to 15 μm.

was set to 15 μm, resulting in 3,401,965 C3D10 (quadratic tetrahedral) elements and 5,277,023 nodes (see Fig. 5). A convergence study on the same lattice specimen has been reported in a previous publication from the authors [55].

The adopted mesh is able to capture larger internal pores existing within the truss; however, as reported in [64], the yield strength of LPBF parts is not affected by the presence of such defects. This could be explained by simulations since the large discrepancies observed between as-designed and as-built geometry plays the major role in defining the yield stress of LPBF lattice structures. In literature, it is well known that the actual geometry coming from μ-CT is a fundamental requirement to accurately capture the mechanical behavior of lattice structures [49,65]. In fact, due to the small geometrical features of these structures, as-built geometry can present pores, powder inclusions an other flaws (especially in down facing surfaces). Therefore, if the original, i.e. the as-designed model, is employed as geometry for analysis non-negligible inaccuracies will be obtained [66,67].

4. Results

4.1. Microstructure

Fig. 6 reports the microstructure of a representative node and truss in both planes i.e., parallel and perpendicular to the building direction. In particular, Fig. 6(a) and (b) report a view of a node and a truss in the longitudinal section, whereas Fig. 6(c) and (d) report a view of a node and a truss in the transverse section. The etching process highlighted the grain texture with an average size between 10 and 50 μm. The micrographic images showed a marked differences in the observed microstructure that can be attributed to the printing strategy. In the plane parallel to the building direction, see Fig. 6(a) and (b), melt pools can be clearly observed. Moreover, in both planes are found process-induces pores, that seem to be localized at the free edge of the samples.

Significant differences are also observed between nodes and trusses. The microstructure of the node is almost totally austenitic at the core, where melt pool boundaries are clearly visible. Martensitic inclusions can be observed in the external regions and can be attributed to the sudden cooling experienced by this region during the manufacturing process. On the contrary, truss micrographs show a more heterogeneous microstructure resulting in columnar structures with the evidence of martensite and δ-ferrite inclusion especially in the plane parallel to the building direction. In particular, these elongated columnar structures, with a size of approximately 50 μm, seem to grow along the truss direction as a consequence of the thermal gradient.

Spherical voids, that can be associated to gas entrapment, can also be observed in Fig. 7. Sub-structures can be also observed in the high magnification images as shown in Fig. 7. In particular they are characterized by platelet shape in the longitudinal plane (Fig. 7(a) and (b)) and by cellular shape (Fig. 7(c) and (d)), still suggests the existence of martensite phase. In particular, the presence of columnar martensite grains, in the transverse plane of the nodes and trusses, can be observed just in the near edges regions of the samples, as shown in Fig. 7(c)and (d). In this plane, the microstructure is characterized by cellular structures that can be seen as the cross section of the columnar martensite grains growing up along the building direction.

4.2. Macro-scale characterization

Fig. 8(a) reports the force–displacement and the stress–strain response of a bulk LPBF dogbone sample. Fig. 8(a) also reports the obtained macroscale properties in terms of elastic modulus, E, and yielding strength, σ_y. Fig. 8(b), instead, reports the force–displacement and the equivalent stress–strain response of a lattice LPBF dogbone sample. The word equivalent is used as the stress is calculated over the cross sectional area of the lattice. Fig. 8(b) also reports local strain measurement carried out at the node highlighted within the schematic representation of the sample.

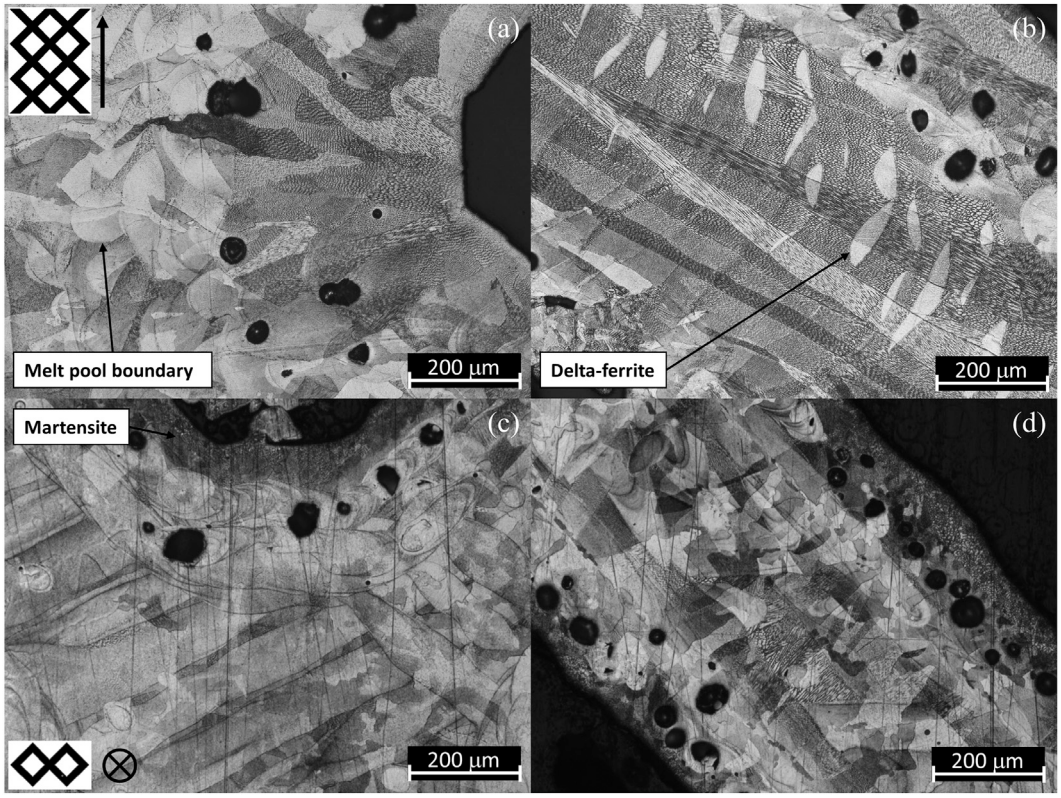

Fig. 6. Etched microstructure of a lattice sample view by optical micrographs investigation: (a) node microstructure in longitudinal section, (b) truss microstructure in longitudinal section, (c) node microstructure in transverse section, (d) truss microstructure in transverse section.

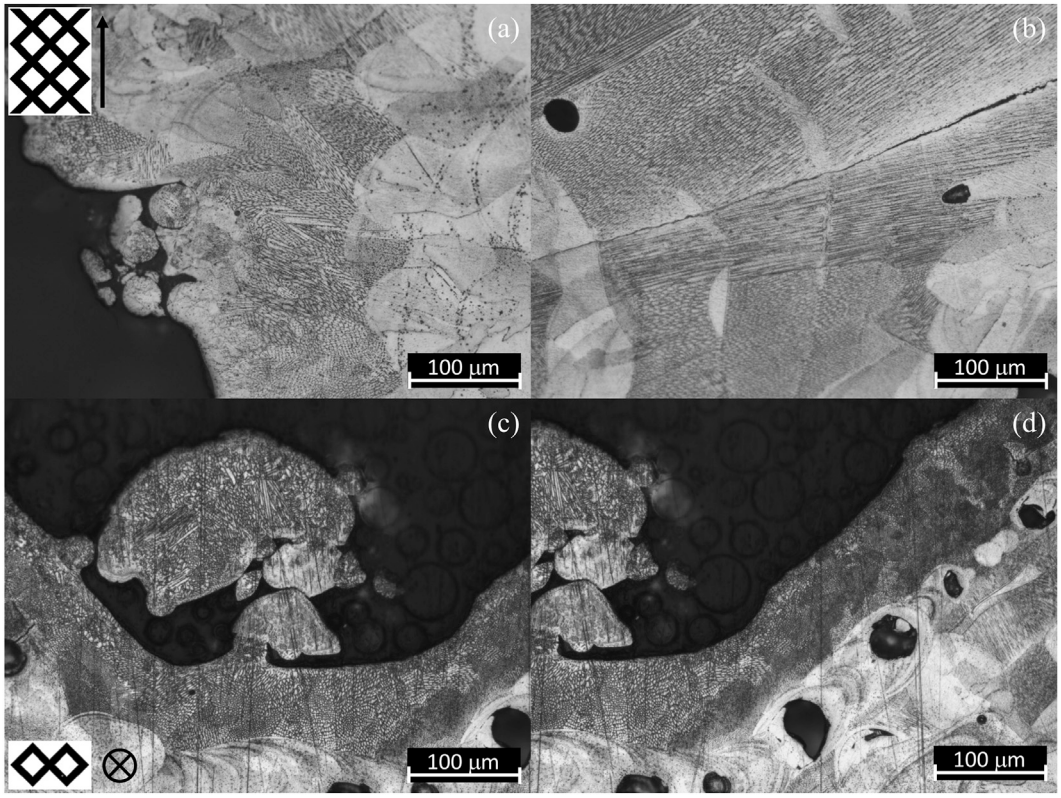

Fig. 7. Etched microstructure of the lattice sample at higher magnification: (a) node microstructure in longitudinal section, (b) truss microstructure in longitudinal section, (c) node microstructure in transverse section, (d) truss microstructure in transverse section.

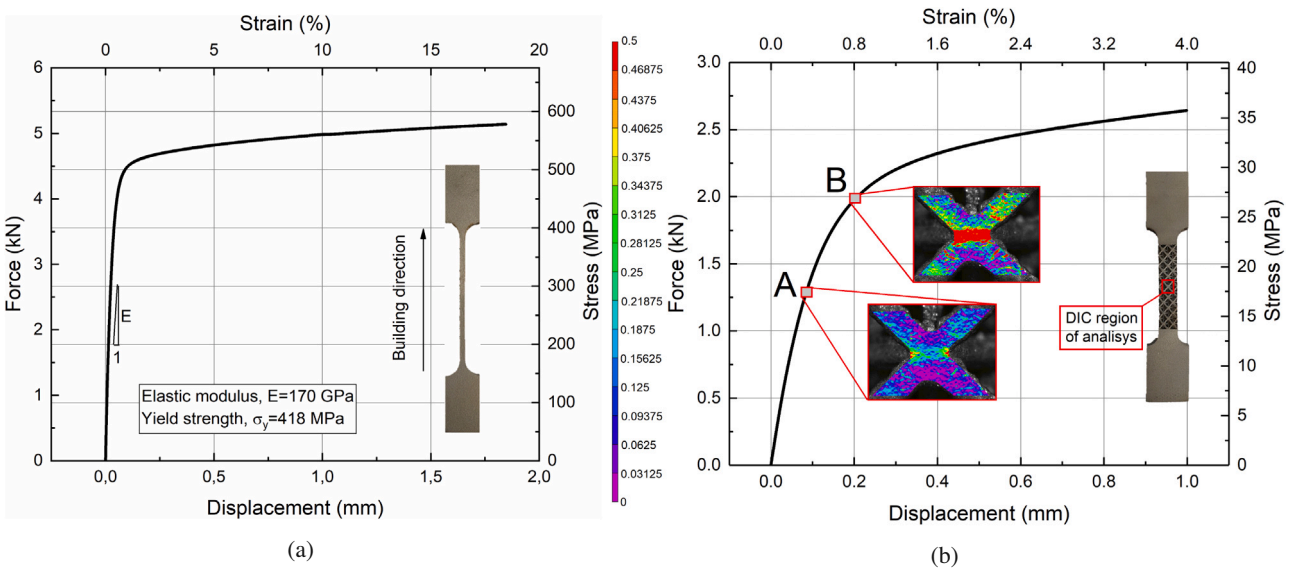

Fig. 8. (a) Stress–strain response of a bulk LPBF dogbone sample; (b) Stress–strain response of a lattice LPBF dogbone sample.

Results show marked difference between the mechanical response of the bulk and the lattice sample. In fact, the former exhibits a sharp change in response moving from the elastic region to the plastic flow. The latter, instead, shows a gradual change in the force–displacement response. Local measurements provide an explanation of this behavior. In fact, results reported in Fig. 8(b) show that, even though the mechanical response of the lattice sample seems to be still elastic at the macroscale, the material is experiencing plastic deformation (see point A in Fig. 8(b)) generating a gradual change in the slope of the force–displacement curve. When the mechanical response starts to highly deviate from linearity (see point B in Fig. 8(b)) local measurements show that the investigated node is completely plastically deformed.

It is important to observe that, due to the heterogeneous microstructure generated by the manufacturing process, as reported in Section 4.1, local mechanical response could be different from the node to the truss. Therefore, the obtained global response, reported in Fig. 8, has to be considered an average response of nodes and trusses. Accordingly, an accurate analysis, from a nanoscale point of view, is required when dealing with lattice structures, as reported in next section.

4.3. Nano-scale characterization

Fig. 9 reports the load vs. indentation depth of the nano-indentation test carried out on the bulk LPBF printed material. The authors would like to remark that the reported curve is the average response of 100 indentations, as discussed in Section 2.3.

Results obtained in Section 4.2 were used to calibrate the value of the constant k, see Eq. (5), that correlates the yield strength, measured by the monotonic tensile test, see Fig. 8(a), with the measured nano-hardness of the bulk material. Considering a yield stress σ_y = 418 MPa and a nano-hardness HV_{IT} = 296 Vickers, a value of the constant k = 1.41 has been obtained.

Fig. 10 shows nanoindentation responses, corresponding to the average data of 100 measurements, obtained from tests carried out on the lattice sample. In particular, Fig. 10(a) presents a comparison between the indentation response measured at the node and the truss along the transverse section. Results show that no remarkable differences exist. Fig. 10(b), instead, reports a comparison between the indentation response measured at the node and the truss along the longitudinal direction. In this case, a systematic reduction of both maximum and residual indentation depths, h_m and h_r, is observed.

Nano-hardness and Young's modulus, calculated from nanoindentation curves on truss and node, are reported in Table 3 for both the analyzed sections. Table 3 also reports the yield strength values estimated on the truss and node by Eq. (5) in both analyzed plane.

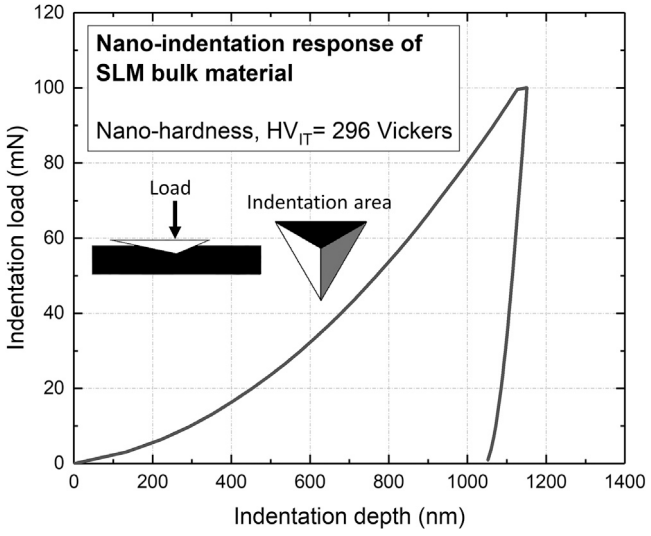

Fig. 9. Nano-indentation response on the bulk material with a maximum indentation load equal to 100 mN.

On the transverse section, no significant differences in terms of nano-hardness and consequently in the yield strength were obtained. In fact, as shown in Fig. 10(a), residual indentation depths are quite similar in both truss and node. In the unloading path of the curve, instead, a steeper slope is obtained on the node, resulting in bigger value of the Young's modulus compared to the truss.

Contrary, remarkable differences in the nano-indentation responses are obtained on the longitudinal sections, in which a marked reduction of both maximum and residual penetration depth results in significant variation of the indentation hardness and elastic modulus. In fact, hardness increases from 231 ± 36.6 Vickers in the truss to 268.3 ± 22.9 Vickers in the node and the elastic modulus increases from 135.3 ± 11.8 GPa to 204.7 ± 14.4 GPa. As a consequence, the estimated yield strength measured on truss and node varies from 326.3 ± 32.2 MPa to 379.2 ± 32.4 MPa, respectively.

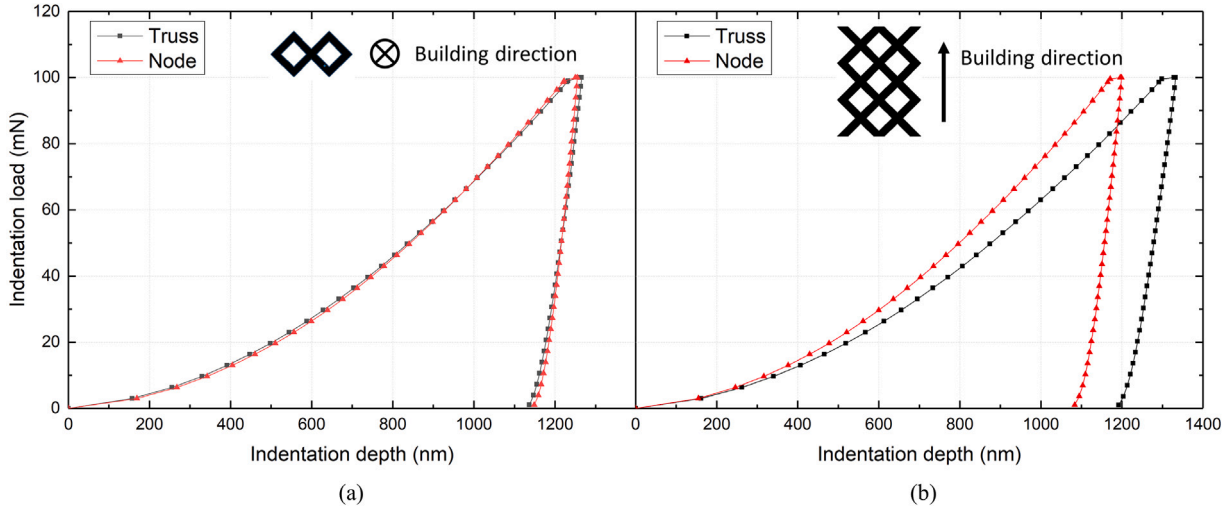

Fig. 10. Nano-indentation response for node and the truss in both plane analyzed: (a) perpendicular to the building direction and (b) parallel to the building direction.

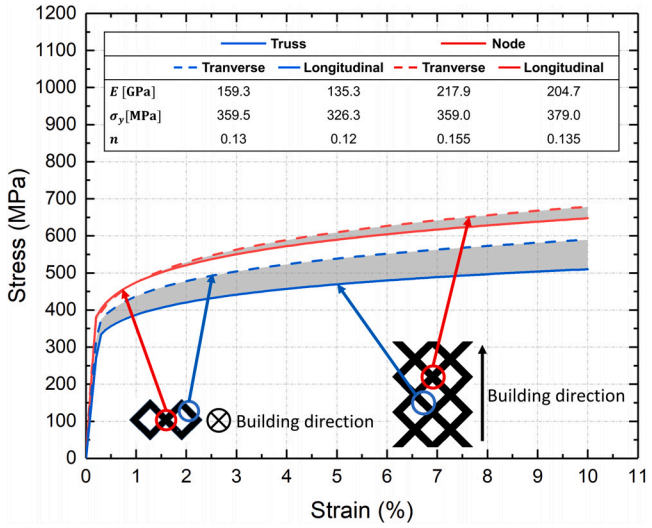

Fig. 11. Comparison between stress–strain curves on node and truss in the longitudinal plane calculated estimated from indentation data. (For interpretation of the references to color in this figure legend, the reader is referred to the web version of this article.)

5. Discussion

5.1. Microstructural analysis

The observed columnar structures tend to grow up extending the consecutive layers as clearly shown in Fig. 6(b) and (d). This behavior can be considered as a consequence of the epitaxial growth of the grains [68], in fact, during solidification, grains tend to grow epitaxially in correspondence of those solidified grains and along the direction normal to the fusion plane. This surface, in fact, is energetically favorite for crystallization [68] so solidification within the melt pool occurs epitaxially along the melt pool boundaries where partially melted grains can be found. In addition, also the heat flux influences the growth direction of the grains, that tend to growth perpendicularly to the solidified planar grains (see Fig. 6(b)). In this regard, process-induced pores may be formed when a lack of residual melt is found between two o more solidified grains.

Regarding the formation of process-induced pores, two main mechanisms could be associated to this phenomenon, i.e. insufficient laser energy during the LPBF process leading to incomplete melting of powder [69], or balling [70]. The latter, in fact, occurs when the high viscosity or the high wetting angle of the molten track results in agglomerates of ellipsoidal and/or spherical metallic balls that tend to be formed to minimize the surface energy. Since the process continues with the successive deposition of the new powder, the new layer is not able to fill the irregularities generated by balling, whereas laser energy is not enough to melt the new layer that tend to be thicker than the previous one. As a consequence, it can be concluded that, during LPBF process, pores and defects are formed as a consequence of the incomplete melting of the 316L precursor particles, because their shape and size are of the same order of the particles diameter of the starting powders and they tend to form in correspondence of the grain boundaries as highlighted by the micrographs.

In this regard, the analyzed samples cannot be considered almost fully dense. Nevertheless, it can be pointed out that the observed pores have spherical shape and dimension of 50 μm at most, in particular, voids associated to gas entrapment generally are in the range 10–20 μm. In addition, they are localized just in the external region of the trusses, while nodes are almost fully dense. Several works [71–73] reported how this kind of pores does not have a significant influence on the stress–strain response of the AM 316L except in the branch beyond the necking occurrence, that has not been analyzed in this research.

5.2. Constitutive behavior estimation

Indentation data were employed to estimate the $\sigma - \epsilon$ response of the AM SS 316L in both planes. In this regard, the previously described approach allows to take into account the anisotropy induced by the process as highlighted by both micrographs and indentation tests. In particular, the strain hardening exponent of the plastic flow has been estimated using the model proposed by Dao et al. [61] and explained in Section 3.1, resulting in n = 0.12 and n = 0.145 for truss and node, respectively, in the longitudinal plane and n = 0.13 and n = 0.155, respectively, in the traverse section.

Fig. 11 reports the stress–strain response of truss and node calculated by the nanoindentation based approach. Slight differences can be observed on the $\sigma - \epsilon$ responses calculated at the node in the transverse and longitudinal section (dashed red curve and continuous red curve respectively). In fact, micrographic analysis shows an almost homogeneous microstructure at the center of the node characterized by austenitic phase, even though the evidence of melt pool boundaries suggests the presence of preferred growth direction induced by the scanning strategy. Such preferential growth directions are responsible

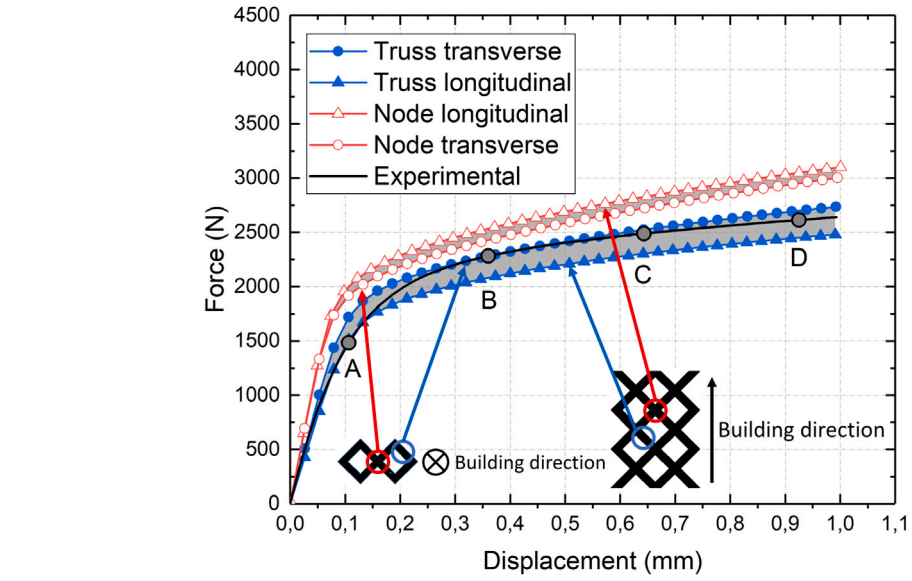

(a)

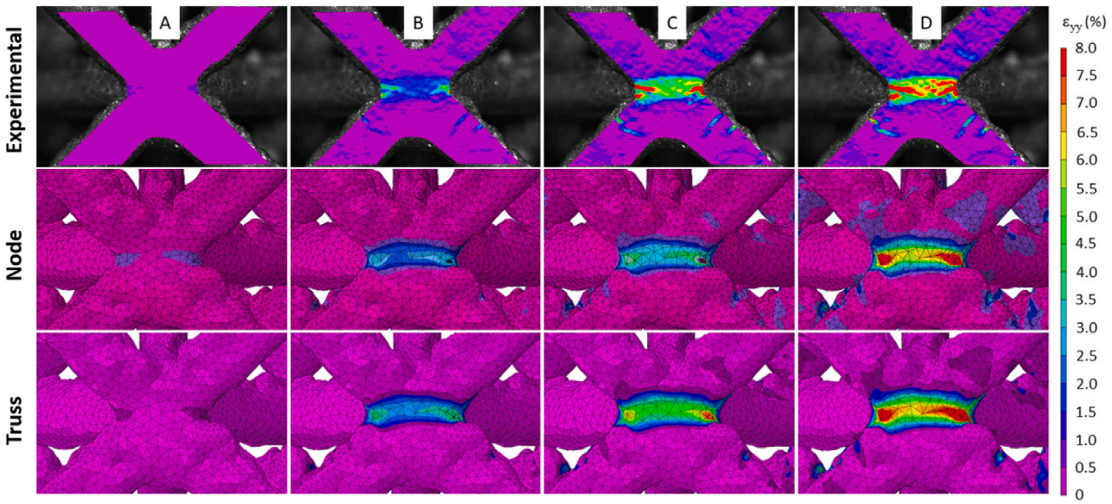

(b)

Fig. 12. Comparison between force–displacement curves (a) and between experimental DIC and numerical strain maps (b) from experimental and numerical uniaxial tensile test from as-built geometry with both $\sigma - \epsilon$ response calculated on node and truss in the longitudinal plane with a mesh tolerances equal to 15 μm. (For interpretation of the references to color in this figure legend, the reader is referred to the web version of this article.)

for the observed differences in the material's behavior in the two analyzed planes.

On the contrary, a marked difference has been observed in the $\sigma - \epsilon$ responses calculated for the truss in both planes and highlighted by the blue curves. In this case, the micrographs reported Section 4.1 present a more complex microstructure with significant differences. In particular, the microstructure is characterized by columnar grains, with evidence of δ-ferrite inclusions, that tend to grow in the plane parallel to the building direction, as highlighted in Fig. 6(b) and (d). The presence of inclusions in a large number of grain boundaries are responsible for a more rigid response of the material during the indentation. As a consequence, the estimated value of the elastic modulus, E, yield strength, σ_y, and hardening exponent, n, tend to increase in the transverse section if compared with the longitudinal one.

5.3. Experimental validation

Fig. 12(a) reports the force–displacement curves obtained from experiments and finite element simulations. The black curve represents the mechanical response measured from the bulk dog-bone sample, whereas the red and blue ones are the numerical responses obtained from finite element analysis when the constitutive behavior, measured by nanoindentation approach, is used, see Section 3.1. In particular, red curve is the numerical force–displacement response obtained from the stress–strain behavior estimated on the truss, whereas blue curve is the numerical force–displacement response obtained from the stress–strain behavior estimated on the node. It can be noted that, if the mechanical behavior calculated on the trusses in both planes is used, the experimental curve well fits numerical results. On the contrary, a slight difference can be observed using the $\sigma - \epsilon$ curves calculated on the node.

This result can be explained analyzing more in detail the lattice geometry. It can be assessed that the weakest regions in terms of stiffness are represented by the trusses. This region, in fact, experience larger displacements, dominating the global response of the lattice structure. This aspect motivates why the best fitting between the numerical and experimental force–displacement response was found using the mechanical behavior estimated on the trusses.

Table 3
Average values of nano-hardness, Young's modulus and Yield strength estimated by nano-indentation measurements.

	Truss		Node	
	Transverse	Longitudinal	Transverse	Longitudinal
Nano-hardness [Vickers]	254.5 ± 22.8	231.0 ± 36.6	254.1 ± 21.5	268.3 ± 22.9
Young's modulus [GPa]	159.3 ± 13.2	135.3 ± 11.8	217.9 ± 15.2	204.7 ± 14.4
Yield strength [MPa]	359.5 ± 32.2	326.3 ± 51.7	359.0 ± 30.4	379.0 ± 32.4

Table A.1
Constant parameters (α_i) of the dimensionless function Π_α.

−1.131	13.635	−30.594	29.267

Table A.2
Constant parameters (β_{ij}) of the dimensionless function Π_β.

−1.40557	0.77526	0.1583	−0.06831
17.93006	−9.22091	−2.37733	0.86295
−79.99715	40.5562	9.00157	−2.54543
122.65069	−63.88418	−9.58936	6.20045

Previous conclusion was also validated by local analyses, as reported in Fig. 12(b) where the strain maps obtained both experimentally, by DIC measurements, and numerically, using the constitutive $\sigma - \epsilon$ response estimated by indentation measurements, are reported. Results show that strain values, both numerically and experimentally, are higher within the nodes than the trusses because of the strain concentration induced by the particular geometry of the node (see Fig. 12(b)). In such region, in fact, strains locally reach values up to 8% when a displacement of 1 mm is applied to the lattice sample. Furthermore, good agreement between numerical and experimental local strains has been found, as confirmed by the numerical maps observed by using the mechanical properties measured on the trusses that show a most accurate match with the DIC data for all the investigated force level (points A–D in Fig. 12(b)).

This result confirms that the as-built geometry, obtained from micro-CT images, combined with the local mechanical behavior has a non-negligible influence on the accuracy of the numerical simulation. In fact, $in-situ$ nano-indentation measurements are able to capture the influence of extremely local features, such as the microstructure modification induced by the different cooling rate linked to the geometry of the lattice structure that significantly affects the global response.

Therefore, the proposed approach allows to obtain the most accurate mechanical predictions compared to the ones obtained using the as-designed geometry and constitutive response measured from a LPBF bulk sample. In fact, as reported in a previous work by the authors [55], if the bulk constitutive response is employed together with the actual geometry of the sample obtained from μ-CT images, non-negligible error, in the order of 21% at 1 mm of displacement, is obtained. In addition, it was shown that the experimental curve starts yielding at lower values if compared to the simulated as-built geometry curve.

6. Conclusion

In the present work a novel methodology, based on a multi-scale approach, for the prediction of the mechanical behavior of octet-truss lattice structure made by LPBF technology was proposed.

To this aim, a finite element numerical model was implemented based on the real geometry of the lattice sample and the local constitutive response of the material. The actual geometry of the sample, that is different from the nominal one, was reconstructed by μ-CT data, whereas local mechanical properties were estimated by a nanoindentation-based approach.

In lattice structure, in fact, the knowledge of the local behavior is extremely important because, as observed from micrographic analyses, LPBF process highly influences the microstructure evolution of trusses and nodes. This difference is induced by different cooling rate and it has been shown having a strong effect on the global force–displacement response of the lattice structure. In fact, if the stress–strain constitutive behavior, obtained from bulk sample, is used, a big mismatch between the experimental and numerical response of the lattice sample will be obtained.

Results revealed that only if the actual geometry of the sample is modeled and the constitutive behavior obtained from local measurements is implemented, the numerical response of the lattice structure well predicts the experimental one. The proposed approach was also validated by comparing the local strain of a node, calculated by the finite element simulations, with the experimentally measured one, that are obtained with the digital image correlation technique.

The presented results give a novel insight on the complex process–structure–properties relationship of LPBF lattice structure, opening the possibility for a better control and reproducibility of LPBF products. As further outlook of the present work, different types of lattice structures and AM materials will be investigated.

CRediT authorship contribution statement

Pietro Magarò: Conceptualization, Methodology, Investigation, Visualization, Writing – original draft. **Gianluca Alaimo:** Resources, Conceptualization, Formal analysis, Data curation, Visualization, Writing – review & editing. **Massimo Carraturo:** Conceptualization, Validation, Software, Investigation, Writing – review & editing. **Emanuele Sgambitterra:** Conceptualization, Software, Validation, Visualization, Writing – review & editing. **Carmine Maletta:** Conceptualization, Supervision, Writing – review & editing.

Declaration of competing interest

The authors declare that they have no known competing financial interests or personal relationships that could have appeared to influence the work reported in this paper.

Data availability

Data will be made available on request.

Acknowledgments

This work was partially supported by the Italian Minister of University and Research through the MIUR-PRIN project "A BRIDGE TO THE FUTURE" (No. 2017L7X3CS).

Nanoindentation experiments, tensile tests and full-field measurements were carried out in the "MaTeRiA Laboratory" (University of Calabria), funded with "Pon Ricerca e Competitività 2007/2013".

Appendix

In this appendix constant parameters of the dimensionless functions depending on the indenter geometry identified in Section 3.1.2 are listed explicitly (see Tables A.1 and A.2).

References

[1] T. Maconachie, M. Leary, B. Lozanovski, X. Zhang, M. Qian, O. Faruque, M. Brandt, SLM lattice structures: Properties, performance, applications and challenges, Mater. Des. 183 (2019) 108–137, http://dx.doi.org/10.1016/j.matdes.2019.108137.

[2] L. Hao, D. Raymont, C. Yan, A. Hussein, P. Young, Design and additive manufacturing of cellular lattice structures, in: Innovative Developments in Virtual and Physical Prototyping, 2011, http://dx.doi.org/10.1201/b11341-40.

[3] A.A. Zadpoor, Acta Biomaterialia Mechanical performance of additively manufactured meta-biomaterials, Acta Biomater. 85 (2019) 41–59, http://dx.doi.org/10.1016/j.actbio.2018.12.038.

[4] S. Duan, W. Wen, D. Fang, Additively-manufactured anisotropic and isotropic 3D plate-lattice materials for enhanced mechanical performance: Simulations and experiments, Acta Mater. 199 (2020) 397–412, http://dx.doi.org/10.1016/j.actamat.2020.08.063.

[5] A. Mertens, S. Reginster, H. Paydas, Q. Contrepois, T. Dormal, O. Lemaire, Mechanical properties of alloy Ti – 6Al – 4V and of stainless steel 316L processed by selective laser melting: influence of out-of-equilibrium microstructures, Powder Metall. 57 (3) (2014) 184–189, http://dx.doi.org/10.1179/1743290114Y.0000000092.

[6] A.E. Wilson-Heid, S. Qin, A.M. Beese, Multiaxial plasticity and fracture behavior of stainless steel 316L by laser powder bed fusion: Experiments and computational modeling, Acta Mater. 199 (2020) 578–592, http://dx.doi.org/10.1016/j.actamat.2020.08.066.

[7] P. Kumar, R. Jayaraj, J. Suryawanshi, U. Satwik, J. McKinnell, U. Ramamurty, Fatigue strength of additively manufactured 316L austenitic stainless steel, Acta Mater. 199 (2020) 225–239, http://dx.doi.org/10.1016/j.actamat.2020.08.033.

[8] F. Calignano, D. Manfredi, E.P. Ambrosio, L. Iuliano, P. Fino, Influence of process parameters on surface roughness of aluminum parts produced by DMLS, Int. J. Adv. Manuf. Technol. 67 (2013) 2743–2751, http://dx.doi.org/10.1007/s00170-012-4688-9.

[9] C. Qiu, C. Panwisawas, M. Ward, H.C. Basoalto, J.W. Brooks, M.M. Attallah, On the role of melt flow into the surface structure and porosity development during selective laser melting, Acta Mater. 96 (2015) 72–79, http://dx.doi.org/10.1016/j.actamat.2015.06.004.

[10] S.A. Khairallah, A.T. Anderson, A. Rubenchik, W.E. King, Laser powder-bed fusion additive manufacturing: Physics of complex melt flow and formation mechanisms of pores, spatter, and denudation zones, Acta Mater. 108 (2016) 36–45, http://dx.doi.org/10.1016/j.actamat.2016.02.014.

[11] A. Riemer, S. Leuders, M. Thöne, H.A. Richard, T. Tröster, T. Niendorf, On the fatigue crack growth behavior in 316L stainless steel manufactured by selective laser melting, Eng. Fract. Mech. 120 (2014) 15–25, http://dx.doi.org/10.1016/j.engfracmech.2014.03.008.

[12] J. Suryawanshi, K.G. Prashanth, U. Ramamurty, Mechanical behavior of selective laser melted 316L stainless steel, Mater. Sci. Eng. A 696 (April) (2017) 113–121, http://dx.doi.org/10.1016/j.msea.2017.04.058.

[13] T.M. Mower, M.J. Long, Mechanical behavior of additive manufactured, powder-bed laser-fused materials, Mater. Sci. Eng. A 651 (2016) 198–213, http://dx.doi.org/10.1016/j.msea.2015.10.068.

[14] M. Awd, F. Stern, A. Kampmann, D. Kotzem, J. Tenkamp, F. Walther, Microstructural characterization of the anisotropy and cyclic deformation behavior of selective laser melted AlSi10Mg structures, Metals 8 (10) (2018) 825, http://dx.doi.org/10.3390/met8100825.

[15] A.F. Chadwick, P.W. Voorhees, The development of grain structure during additive manufacturing, Acta Mater. 211 (2021) 116862, http://dx.doi.org/10.1016/j.actamat.2021.116862.

[16] M. Shamsujjoha, S.R. Agnew, J.M. Fitz-Gerald, W.R. Moore, T.A. Newman, High strength and ductility of additively manufactured 316L stainless steel explained, Metall. Mater. Trans. A 49 (7) (2018) 3011–3027, http://dx.doi.org/10.1007/s11661-018-4607-2.

[17] Z. Sun, X. Tan, S.B. Tor, W.Y. Yeong, Selective laser melting of stainless steel 316L with low porosity and high build rates, Mater. Des. 104 (2016) 197–204, http://dx.doi.org/10.1016/j.matdes.2016.05.035.

[18] Y.M. Wang, T. Voisin, J.T. Mckeown, J. Ye, N.P. Calta, Z. Li, Z. Zeng, Y. Zhang, W. Chen, T.T. Roehling, R.T. Ott, M.K. Santala, P.J. Depond, M.J. Matthews, A.V. Hamza, T. Zhu, Additively manufactured hierarchical stainless steels with high strength and ductility, Nature Mater. 17 (January) (2018) 63–71, http://dx.doi.org/10.1038/NMAT5021.

[19] K. Saeidi, X. Gao, F. Lofaj, L. Kvetková, Z. Shen, Transformation of austenite to duplex austenite-ferrite assembly in annealed stainless steel 316L consolidated by laser melting, J. Alloys Compd. 633 (2015) 463–469, http://dx.doi.org/10.1016/j.jallcom.2015.01.249.

[20] Z. Li, T. Voisin, J.T. Mckeown, J. Ye, T. Braun, C. Kamath, W.E. King, Y.M. Wang, Tensile properties , strain rate sensitivity , and activation volume of additively manufactured 316L stainless steels, Int. J. Plast. 120 (October 2018) (2019) 395–410, http://dx.doi.org/10.1016/j.ijplas.2019.05.009.

[21] T.R. Smith, J.D. Sugar, C. San, J.M. Schoenung, Strengthening mechanisms in directed energy deposited austenitic stainless steel, Acta Mater. 164 (2019) 728–740, http://dx.doi.org/10.1016/j.actamat.2018.11.021.

[22] K. Saeidi, X. Gao, Y. Zhong, Z.J. Shen, Hardened austenite steel with columnar sub-grain structure formed by laser melting, Mater. Sci. Eng. A 625 (2015) 221–229, http://dx.doi.org/10.1016/j.msea.2014.12.018.

[23] J.R. Trelewicz, G.P. Halada, O.K. Donaldson, G. Manogharan, Microstructure and corrosion resistance of laser additively manufactured 316L stainless steel, JOM 68 (3) (2016) 850–859, http://dx.doi.org/10.1007/s11837-016-1822-4.

[24] M. Ziętala, T. Durejko, M. Polański, I. Kunce, T. Płociński, W. Zieliński, M. Łazińska, W. Stępniowski, T. Czujko, K.J. Kurzydłowski, Z. Bojar, The microstructure, mechanical properties and corrosion resistance of 316 L stainless steel fabricated using laser engineered net shaping, Mater. Sci. Eng. A 677 (2016) 1–10, http://dx.doi.org/10.1016/j.msea.2016.09.028.

[25] Z. Li, B. He, Q. Guo, Strengthening and hardening mechanisms of additively manufactured stainless steels: The role of cell sizes, Scr. Mater. 177 (2020) 17–21, http://dx.doi.org/10.1016/j.scriptamat.2019.10.005.

[26] S.R. Agnew, J.M. Fitz-gerald, W.R. Moore, T.A. Newman, High strength and ductility of additively manufactured 316L stainless steel explained, Metall. Mater. Trans. A 49 (7) (2018) 3011–3027, http://dx.doi.org/10.1007/s11661-018-4607-2.

[27] X. Wang, J.A. Muñiz-lerma, O. Sánchez-mata, M.A. Shandiz, Microstructure and mechanical properties of stainless steel 316L vertical struts manufactured by laser powder bed fusion process, Mater. Sci. Eng. A 736 (August) (2018) 27–40, http://dx.doi.org/10.1016/j.msea.2018.08.069.

[28] S.-h. Sun, K. Hagihara, T. Nakano, Effect of scanning strategy on texture formation in Ni-25 at .% Mo alloys, Mater. Des. 140 (2018) 307–316, http://dx.doi.org/10.1016/j.matdes.2017.11.060.

[29] M.L. Montero-Sistiaga, M. Godino-Martinez, K. Boschmans, J.-P. Kruth, J. Van Humbeeck, K. Vanmeensel, Microstructure evolution of 316L produced by HP-SLM (high power selective laser melting), Addit. Manuf. 23 (2018) 402–410, http://dx.doi.org/10.1016/j.addma.2018.08.028.

[30] U.S. Bertoli, B.E. Macdonald, J.M. Schoenung, Stability of cellular microstructure in laser powder bed fusion of 316L stainless steel, Mater. Sci. Eng. A 739 (October 2018) (2019) 109–117, http://dx.doi.org/10.1016/j.msea.2018.10.051.

[31] X. Wang, J. Alberto, M. Lerma, O. Sanchez, M. Sıla, E. Atabay, Single – crystalline – like stainless steel 316L with different geometries fabricated by laser powder bed fusion, Prog. Addit. Manuf. 5 (1) (2020) 41–49, http://dx.doi.org/10.1007/s40964-020-00123-9.

[32] S.-H. Sun, T. Ishimoto, K. Hagihara, Y. Tsutsumi, T. Hanawa, T. Nakano, Excellent mechanical and corrosion properties of austenitic stainless steel with a unique crystallographic lamellar microstructure via selective laser melting, Scr. Mater. 159 (2019) 89–93, http://dx.doi.org/10.1016/j.scriptamat.2018.09.017.

[33] S. Bahl, S. Mishra, K. Yazar, I.R. Kola, K. Chatterjee, S. Suwas, Non-equilibrium microstructure, crystallographic texture and morphological texture synergistically result in unusual mechanical properties of 3D printed 316L stainless steel, Addit. Manuf. 28 (2019) 65–77, http://dx.doi.org/10.1016/j.addma.2019.04.016.

[34] U. Scipioni Bertoli, A.J. Wolfer, M.J. Matthews, J.-P.R. Delplanque, J.M. Schoenung, On the limitations of volumetric energy density as a design parameter for selective laser melting, Mater. Des. 113 (2017) 331–340, http://dx.doi.org/10.1016/j.matdes.2016.10.037.

[35] J. Plocher, A. Panesar, Review on design and structural optimisation in additive manufacturing: Towards next-generation lightweight structures, Mater. Des. 183 (2019) 108164, http://dx.doi.org/10.1016/j.matdes.2019.108164.

[36] D. Mahmoud, M.A. Elbestawi, Lattice structures and functionally graded materials applications in additive manufacturing of orthopedic implants: A review, J. Manuf. Mater. Process. 1 (2) (2017) http://dx.doi.org/10.3390/jmmp1020013.

[37] S. Piazza, B. Merrigan, D.P. Dowling, M. Celikin, The effects of geometry and laser power on the porosity and melt pool formation in additively manufactured 316L stainless steel, Int. J. Adv. Manuf. Technol. 111 (5–6) (2020) 1457–1470, http://dx.doi.org/10.1007/s00170-020-06196-8.

[38] G. Mohr, N. Scheuschner, K. Hilgenberg, In situ heat accumulation by geometrical features obstructing heat flux and by reduced inter layer times in laser powder bed fusion of AISI 316L stainless steel, Procedia CIRP 94 (2020) 155–160, http://dx.doi.org/10.1016/j.procir.2020.09.030, 11th CIRP Conference on Photonic Technologies [LANE 2020].

[39] S. Siddique, M. Imran, M. Rauer, M. Kaloudis, E. Wycisk, C. Emmelmann, F. Walther, Computed tomography for characterization of fatigue performance of selective laser melted parts, Mater. Des. 83 (2015) 661–669, http://dx.doi.org/10.1016/j.matdes.2015.06.063.

[40] X. Cai, A.A. Malcolm, B.S. Wong, Z. Fan, Measurement and characterization of porosity in aluminium selective laser melting parts using X-ray CT, Virtual Phys. Prototyp. 10 (4) (2015) 195–206, http://dx.doi.org/10.1080/17452759.2015.1112412.

[41] W.W. Wits, S. Carmignato, F. Zanini, T.H.J. Vaneker, Porosity testing methods for the quality assessment of selective laser melted parts, CIRP Ann. - Manuf. Technol. 65 (1) (2016) 201–204, http://dx.doi.org/10.1016/j.cirp.2016.04.054.

[42] G. Kasperovich, J. Haubrich, J. Gussone, G. Requena, Correlation between porosity and processing parameters in TiAl6V4 produced by selective laser melting, JMADE 105 (2016) 160–170, http://dx.doi.org/10.1016/j.matdes.2016.05.070.

[43] Y. Amani, S. Dancette, P. Delroisse, A. Simar, E. Maire, Compression behavior of lattice structures produced by selective laser melting: X-ray tomography based experimental and finite element approaches, Acta Mater. 159 (2018) 395–407, http://dx.doi.org/10.1016/j.actamat.2018.08.030.

[44] C. Qiu, N.J.E. Adkins, M.M. Attallah, Microstructure and tensile properties of selectively laser-melted and of HIPed laser-melted Ti – 6Al – 4V, Mater. Sci. Eng. A 578 (2013) 230–239, http://dx.doi.org/10.1016/j.msea.2013.04.099.

[45] R. Ganeriwala, M. Strantza, W. King, B. Clausen, T. Phan, L. Levine, D. Brown, N. Hodge, Evaluation of a thermomechanical model for prediction of residual stress during laser powder bed fusion of Ti-6Al-4V, Addit. Manuf. 27 (2019) 489–502, http://dx.doi.org/10.1016/j.addma.2019.03.034.

[46] M. Carraturo, J. Jomo, S. Kollmannsberger, A. Reali, F. Auricchio, E. Rank, Modeling and experimental validation of an immersed thermo-mechanical part-scale analysis for laser powder bed fusion processes, Addit. Manuf. 36 (2020) 101498, http://dx.doi.org/10.1016/j.addma.2020.101498.

[47] L. Boniotti, S. Beretta, S. Foletti, L. Patriarca, Strain concentrations in BCC micro lattices obtained by AM, Procedia Struct. Integr. 7 (2017) 166–173, http://dx.doi.org/10.1016/j.prostr.2017.11.074.

[48] L. Boniotti, S. Foletti, S. Beretta, L. Patriarca, Analysis of strain and stress concentrations in micro-lattice structures manufactured by SLM, Rapid Prototyp. J. (2019) 370–380, http://dx.doi.org/10.1108/RPJ-10-2018-0270.

[49] L. Boniotti, S. Beretta, L. Patriarca, L. Rigoni, S. Foletti, Experimental and numerical investigation on compressive fatigue strength of lattice structures of AlSi7Mg manufactured by SLM, Int. J. Fatigue 128 (2019) 105181, http://dx.doi.org/10.1016/j.ijfatigue.2019.06.041.

[50] W.C. Oliver, G.M. Pharr, Improved technique for determining hardness and elastic modulus using load and displacement sensing indentation experiments, J. Mater. Res. 7 (6) (1992) 1564–1580, http://dx.doi.org/10.1557/JMR.1992.1564.

[51] X. Li, B. Bhushan, A review of nanoindentation continuous stiffness measurement technique and its applications, Mater. Charact. 48 (1) (2002) 11–36, http://dx.doi.org/10.1016/S1044-5803(02)00192-4.

[52] M.D. Uchic, D.M. Dimiduk, A methodology to investigate size scale effects in crystalline plasticity using uniaxial compression testing, Mater. Sci. Eng. A 400–401 (1-2 SUPPL.) (2005) 268–278, http://dx.doi.org/10.1016/j.msea.2005.03.082.

[53] S. Roos, C. Botero, J. Danvind, A. Koptioug, L.. Rännar, Macro- and micromechanical behavior of 316LN lattice structures manufactured by electron beam melting, J. Mater. Eng. Perform. 28 (12) (2019) 7290–7301, http://dx.doi.org/10.1007/s11665-019-04484-3.

[54] W.D. Nix, H. Gao, Indentation size effects in crystalline materials: A law for strain gradient plasticity, J. Mech. Phys. Solids 46 (3) (1998) 411–425, http://dx.doi.org/10.1016/S0022-5096(97)00086-0.

[55] M. Carraturo, G. Alaimo, S. Marconi, E. Negrello, E. Sgambitterra, C. Maletta, A. Reali, F. Auricchio, Experimental and numerical evaluation of mechanical properties of 3D-printed stainless steel 316L lattice structures, J. Mater. Eng. Perform. 30 (2021) 5247–5251, http://dx.doi.org/10.1007/s11665-021-05737-w.

[56] ISO 14577-1:2015, Metallic materials — Instrumented indentation test for hardness and materials parameters — Part 1: Test method.

[57] P. Zhang, S. Li, Z. Zhang, General relationship between strength and hardness, Mater. Sci. Eng. A 529 (2011) 62–73, http://dx.doi.org/10.1016/j.msea.2011.08.061.

[58] M. Gaško, G. Rosenberg, Correlation between hardness and tensile properties in ultra-high strength dual phase steels – short communication, Mater. Eng. 18 (2011) 155–159.

[59] J.R. Cahoon, W.H. Broughton, A.R. Kutzak, The determination of yield strength from hardness measurements, Metall. Trans. 2 (1971) 1979–1983, http://dx.doi.org/10.1007/BF02913433.

[60] E.J. Pavlina, C.J. Van Tyne, Correlation of yield strength and tensile strength with hardness for steels, J. Mater. Eng. Perform. 17 (6) (2008) 888–893, http://dx.doi.org/10.1007/s11665-008-9225-5.

[61] M. Dao, N. Chollacoop, K. Van Vliet, T. Venkatesh, S. Suresh, Computational modeling of the forward and reverse problems in instrumented sharp indentation, Acta Mater. 49 (19) (2001) 3899–3918, http://dx.doi.org/10.1016/S1359-6454(01)00295-6.

[62] F. Kick, Das Gesetz der Proportionalen Widerstände und Seine Anwendungen, Felix-Verlag, Leipzig, 1885.

[63] ABAQUS/Standard User's Manual, Dassault Systèmes Simulia Corp, United States, 2019.

[64] A. Du Plessis, I. Yadroitsava, D. Kouprianoff, I. Yadroitsev, Numerical and experimental study of the effect of artificial porosity in a lattice structure manufactured by laser based powder bed fusion, in: Solid Freeform Fabrication 2018: Proceedings of the 29th Annual International, 2018, pp. 808–820, http://dx.doi.org/10.13140/RG.2.2.28115.84007.

[65] U. Gebhardt, M. Kästner, J. Hufenbach, U. Kühn, M. Berner, S. Holtzhausen, Virtual testing of geometrically imperfect additively manufactured lattice structures, PAMM 20 (2021) http://dx.doi.org/10.1002/pamm.202000090.

[66] N. Korshunova, G. Alaimo, S. Hosseini, M. Carraturo, A. Reali, J. Niiranen, F. Auricchio, E. Rank, S. Kollmannsberger, Image-based numerical characterization and experimental validation of tensile behavior of octet-truss lattice structures, Addit. Manuf. 41 (2021) 101949, http://dx.doi.org/10.1016/j.addma.2021.101949.

[67] N. Korshunova, G. Alaimo, S. Hosseini, M. Carraturo, A. Reali, J. Niiranen, F. Auricchio, E. Rank, S. Kollmannsberger, Bending behavior of octet-truss lattice structures: Modelling options, numerical characterization and experimental validation, Mater. Des. 205 (2021) 109693, http://dx.doi.org/10.1016/j.matdes.2021.109693.

[68] D. Wang, C. Song, Y. Yang, Y. Bai, Investigation of crystal growth mechanism during selective laser melting and mechanical property characterization of 316L stainless steel parts, Mater. Des. 100 (2016) 291–299, http://dx.doi.org/10.1016/j.matdes.2016.03.111.

[69] S. Brown, J. Cherry, H. Davies, S. Mehmood, N. Lavery, J. Sienz, Investigation into the Effect of process parameters on microstructural and physical properties of 316L stainless steel parts by selective laser melting, Int. J. Adv. Manuf. Technol. 76 (5) (2015) 869–879, http://dx.doi.org/10.1007/s00170-014-6297-2.

[70] R. Li, Y. Shi, Z. Wang, L. Wang, J. Liu, W. Jiang, Densification behavior of gas and water atomized 316L stainless steel powder during selective laser melting, Appl. Surf. Sci. 256 (13) (2010) 4350–4356, http://dx.doi.org/10.1016/j.apsusc.2010.02.030.

[71] A. Al-Maharma, S. Patil, B. Markert, Effects of porosity on the mechanical properties of additively manufactured components: a critical review, Mater. Res. Express 7 (2020) 122001, http://dx.doi.org/10.1088/2053-1591/abcc5d.

[72] S. Cacace, L. Pagani, B. Colosimo, Q. Semeraro, The effect of energy density and porosity structure on tensile properties of 316L stainless steel produced by laser powder bed fusion, Prog. Addit. Manuf. 7 (2022) 1–18, http://dx.doi.org/10.1007/s40964-022-00281-y.

[73] W.H. Kan, L. Chiu, S. Lim, Y. Zhu, Y. Tian, D. Jiang, A. Huang, A critical review on the effects of process-induced porosity on the mechanical properties of alloys fabricated by laser powder bed fusion, J. Mater. Sci. 57 (2022) http://dx.doi.org/10.1007/s10853-022-06990-7.